

Plasma Sci. Technol. **24** (2022) 075104 (11pp) https://doi.org/10.1088/2058-6272/ac608f

Simulation studies of tungsten impurity behaviors during neon impurity seeding with tungsten bundled charge state model using SOLPS-ITER on EAST

Shanlu GAO (高善露)[1,2], **Xiaoju LIU** (刘晓菊)[1,*], **Guozhong DENG** (邓国忠)[3], **Tingfeng MING** (明廷凤)[1], **Guoqiang LI** (李国强)[1], **Xuexi ZHANG** (张学习)[1,2], **Xiaodong WU** (吴晓东)[1,2], **Xiaohe WU** (邬潇河)[1,2], **Bang LI** (李邦)[1,2], **Haochen FAN** (樊皓尘)[1,2] **and Xiang GAO** (高翔)[1,3,*]

[1] Institute of Plasma Physics, Hefei Institutes of Physical Science, Chinese Academy of Sciences, Hefei 230031, People's Republic of China
[2] University of Science and Technology of China, Hefei 230026, People's Republic of China
[3] Advanced Energy Research Center, Shenzhen University, Shenzhen 518060, People's Republic of China

E-mail: julie1982@ipp.ac.cn and xgao@ipp.ac.cn

Received 29 November 2021, revised 11 February 2022
Accepted for publication 23 March 2022
Published 29 June 2022

Abstract

An investigation into tungsten (W) impurity behaviors with the update of the EAST lower W divertor for H-mode has been carried out using SOLPS-ITER. This work aims to study the effect of external neon (Ne) impurity seeding on W impurity sputtering with the bundled charge state model. As the Ne seeding rate increases, plasma parameters, W concentration (C_W), and eroded W flux (Γ_W^{Ero}) at both targets are compared and analyzed between the highly resolved bundled model 'jett' and the full W charge state model. The results indicate that 'jett' can produce divertor behaviors essentially in agreement with the full W charge state model. The bundled scheme with high resolution in low W charge states ($<W^{20+}$) has no obvious effect on the Ne impurity distribution and thus little effect on W sputtering by Ne. Meanwhile, parametric scans of radial particle and thermal transport diffusivities ($D_\perp$ and $\chi_{e,i}$) in the SOL are simulated using the 'jett' bundled model. The results indicate that the transport diffusivity variations have significant influences on the divertor parameters, especially for W impurity sputtering.

Keywords: tungsten impurity sputtering, bundled charge state model, transport diffusivity, SOLPS-ITER

(Some figures may appear in colour only in the online journal)

1. Introduction

Tungsten (W) is deemed to be the most promising plasma-facing material (PFM) in modern tokamak devices due to its unique physical properties [1], such as having a high melting point (3683 K), high thermal conductivity, a low fuel retention rate, and a high energy threshold for sputtering [2]. Experimental Advanced Superconducting Tokamak (EAST), a superconducting diverted tokamak, has completed the engineering installation and commissioning phase for the new lower divertor being changed from graphite tiles to W tiles. W, as a high Z impurity, is a strong radiator in core plasma. It tends to accumulate in the core region, while exceeding a certain concentration ($\sim 10^{-5}$) could affect the core confinement and plasma performance.

Active impurity seeding is a favorable choice to reduce the heat load and electron temperature at W targets to an acceptable level by effective power radiation [3]. External

* Authors to whom any correspondence should be addressed.

impurity seeding with nitrogen (N), neon (Ne) and argon (Ar), for example, could influence the plasma behaviors and W impurity transport in tokamaks. The behaviors of W impurity sputtered from targets play critical roles in plasma performance for tokamaks [4, 5].

SOLPS-ITER is considered to be an important tool for studying the W sputtering and transport with external impurity seeding at present, however, it needs a relatively long computational time to reach steady state, especially when considering W impurity with 74 ionization states and external seeding impurity. Various W bundling schemes, including highly resolved and aggressively bundled models, are compared and analyzed in our previous work for different divertor conditions of L-mode on EAST [6]. It indicates that W bundled charge state models provide a marked enhancement in computation speed by a factor of more than five. Besides, it can describe well divertor plasma parameters at targets with a discrepancy of less than 15% for various bundling schemes. It is also found that the discrepancies between net W erosion and deposition are modest among bundled charge state models and full W treatment in ASDEX-Upgrade [7]. However, radiative impurity seeding is not considered in either of these works. To test the reliability of the W bundled model with external impurity seeding, simulation results from the bundled model 'jett' [7] are compared to those of the full W model. Further simulation with the bundled model 'jett' is carried out to study the W target sputtering and W impurity behaviors with transport diffusivity scans during Ne impurity seeding.

The structure of the paper will be as follows. Section 2 comprises the modeling assumptions and brief descriptions of the bundling scheme in SOLPS-ITER code. We mainly focus on the simulation study of W impurity behaviors in section 3 with all W charge state and bundling charge state models respectively. The detailed comparison of W impurity sputtering based on the scan of the Ne puffing rate is also presented in the section. Analysis of the influence of radial particle and thermal diffusivities on W impurity sputtering is included as well. A summary and discussions are presented in section 4.

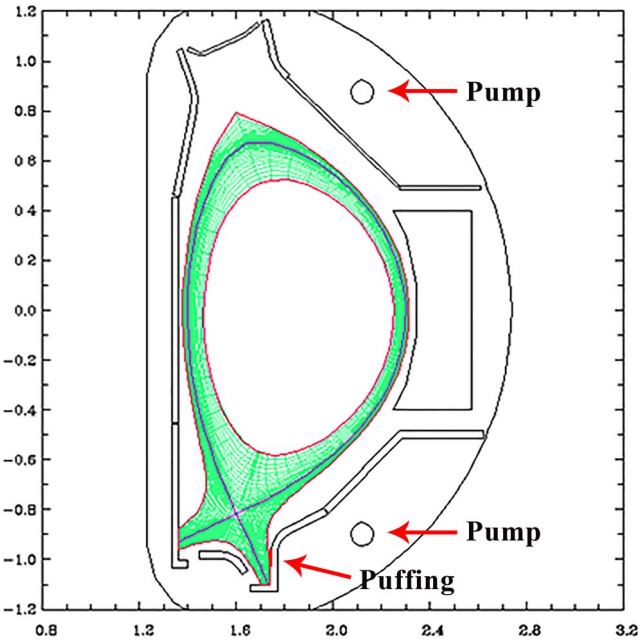

Figure 1. Physical mesh for SOLPS-ITER simulation.

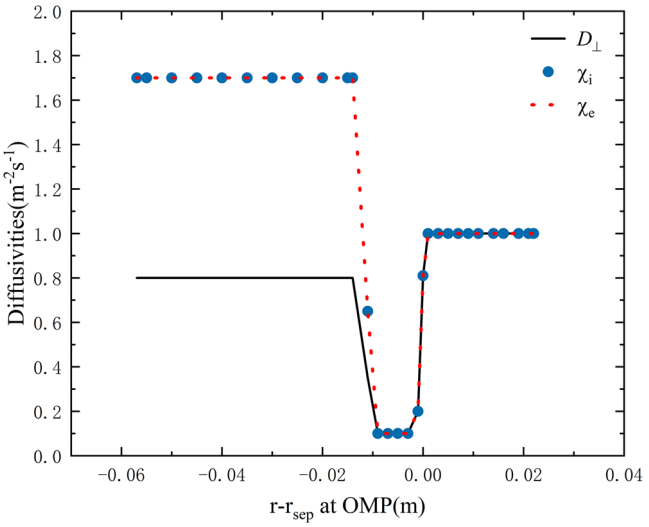

Figure 2. Radial particle and electron/ion thermal diffusivity profiles at OMP.

2. SOLPS-ITER parameter setups

2.1. Boundary conditions and modeling assumptions

SOLPS-ITER [8] is applied for edge plasma simulation, which couples the B2.5 multi-fluid plasma code with EIRENE Monte Carlo neutral transport solver. W and Ne are treated as impurity species in the simulation. The electron, deuterium ion D^+, seeded Ne species (Ne^{1+}, Ne^{2+},⋯, Ne^{10+}) and each ionization state of W (W^{1+}, W^{2+},⋯, W^{74+}) are included in the B2.5 multi-fluid code. EIRENE code handles the transport of neutral particles and solves a series of sources and sinks of energy, particle and momentum, based on the plasma background deduced from B2.5 code. D, D_2, Ne, and W are taken into account for neutral dynamics by EIRENE code [9, 10].

Drift effects ($\boldsymbol{E} \times \boldsymbol{B}$ and diamagnetic) are not included in the simulation due to the massive computation. We select an EAST H-mode equilibrium provided by equilibrium fitting code (EFIT) in this work. Figure 1 shows the physical mesh for SOLPS-ITER simulation and updated lower divertor. The particle diffusivity $D_\perp$ and thermal diffusivity $\chi_e = \chi_i$ profiles along the outer midplane (OMP) are taken as that in figure 2 for H-mode discharge, following the previous simulations for H-mode [11]. The input power entering into the core boundary of the computational region is set to $P_{SOL} = 2.0$ MW. It is divided by electrons and ions evenly.

In SOLPS-ITER code, W source is produced by the physical sputtering from D, Ne and W species at targets based on the standard Roth–Bohdansky model [12]. The particle fluxes of W for each ionization state are set as zero at the

Table 1. Bundling scheme of W.

Model	M0 (All charge states)	M1 (jett)
Species	75	24
Partition numbers	W^{1+}	W^{1+}
	W^{2+}	W^{2+}–W^{4+}
	W^{3+}	W^{5+}
	W^{4+}	W^{6+}
	W^{5+}	W^{7+}
	W^{6+}	W^{8+}
	W^{7+}	W^{9+}
	W^{8+}	W^{10+}–W^{12+}
	W^{9+}	W^{13+}–W^{16+}
	W^{10+}	W^{17+}
	W^{11+}	W^{18+}
	W^{12+}	W^{19+}
	W^{13+}	W^{20+}
	W^{14+}	W^{21+}–W^{22+}
	W^{15+}	W^{23+}–W^{25+}
	…	…
	W^{72+}	W^{41+}–W^{45+}
	W^{73+}	W^{46+}–W^{55+}
	W^{74+}	W^{56+}–W^{74+}

core–edge interface (CEI). We use the SOLPS-ITER version 3.0.7, in which the friction and thermal force terms of impurity transport [13] are deduced from the general Braginskii version of the momentum balance equation rather than using the trace impurity assumption in the previous version [14]. Redeposition [15–17], as an important process for influencing net erosion and plasma confinement, needs to be considered when analyzing the erosion of target material. In our simulation, the redeposition coefficient of W is assumed to be 90% at both targets. Compared with the redeposition coefficient of the EAST experiment, the value selected is more conservative [18].

2.2. Bundled charge state model

The atomic data of the W bundled scheme are from the ADAS data (model of 'year 89') in SOLPS-ITER version 3.0.7. The acceleration of the simulation process after bundling is due to the decrease in the number of conservation equations to be handled. Table 1 shows the scheme of the W bundled model. The numbers shown in the third row represent the partition numbers for the bundled model 'jett', which is considerably reduced. The charge state for the bundled particle is not constant but based on the plasma parameters that affect the ionization balance, such as electron density and temperature. The bundled charge state model can shorten the computation time and computer memory remarkably, especially for the simulation including high Z impurity and external impurity seeding.

M0 is the full W treatment considering all W charge states separately, including 74 W fluids. M1 'jett' is a highly resolved bundled charge state model with 23 W fluids. M1 bundles W ions partially with the better inclusion of W^{1+}–W^{20+}, which are typically dominant in edge plasma. There is no individual charge state above W^{20+} in the M1 model. A highly resolved bundling scheme with more than 20 W fluids could describe the divertor parameters well to a considerable degree [6]. The best approximation of net W erosion is given by the 'jett' scheme compared to the full W treatment [7]. Therefore, we select the relatively optimal bundling model 'jett' in this work.

3. Modeling results and discussion

3.1. Divertor behaviors during Ne impurity seeding

In order to check the discrepancy of plasma behaviors between bundled model 'jett' and the all charge states model to the greatest extent, we introduce external impurity seeding. The simulation results are discussed, which emphasize electron temperature, electron density, particle flux, heat flux, radiation and W sputtering at both divertor targets. For the simulation setups, the deuterium ion density at the CEI is set as $n_{D^+,CEI} = 2.0 \times 10^{19}$ m^{-3}. The atom rate of seeded Ne impurity is fixed at $\Gamma_{Ne} = 1.0 \times 10^{19}$ atoms/s. The low density and seeding rate cause the divertor to operate in the low recycling regime and with high W sputtering, enabling us to better check the accuracy of the 'jett' bundling model. The simulated profiles of electron density (n_e^{OMP}) and electron temperature (T_e^{OMP}) along the OMP are shown in figure 3. The n_e^{OMP} given by 'jett' is virtually consistent with that of the full W treatment shown in figure 3(a). Considering the underestimation of radiation power loss inside the separatrix [6], T_e^{OMP} for 'jett' is a little higher than that of the full W treatment in the core region, but almost the same outside the separatrix.

Figure 4 shows the simulated plasma parameters at both targets, including electron temperature (T_e), heat flux (q_{dep}) and particle flux (Γ_{dep}). Parametric values around the strike point (SP) are higher for 'jett' than for the all W charge states model, which could be explained by the underestimation of radiated power loss, as illustrated in table 2. Compared with the all W charge states model, the peak discrepancies of q_{dep} and T_e in 'jett' are less than 18.5% at the targets. Γ_{dep} differs slightly in figures 4(c) and (f). This indicates that the bundled model 'jett' can describe the divertor parameters well, even for the plasmas under a low recycling regime, when considering the Ne impurity seeding. The discrepancy could be expected to be even smaller in the high recycling regime, according to our previous results [6].

The impurity radiations by both seeded Ne and sputtered W in various subregions, as well as W concentration at the separatrix, are estimated and shown in table 2. The radiation power loss is dominant in the core region, with only a small proportion in the divertor and the SOL region. For radiation power loss by Ne, there is no significant difference between full W treatment and the 'jett' model, elucidating that the bundling scheme 'jett' has little influence on the ionization balance and transport of Ne impurity. It mainly depends on the ionization mean free path and the screening effect from background plasma, which are determined by the parameters

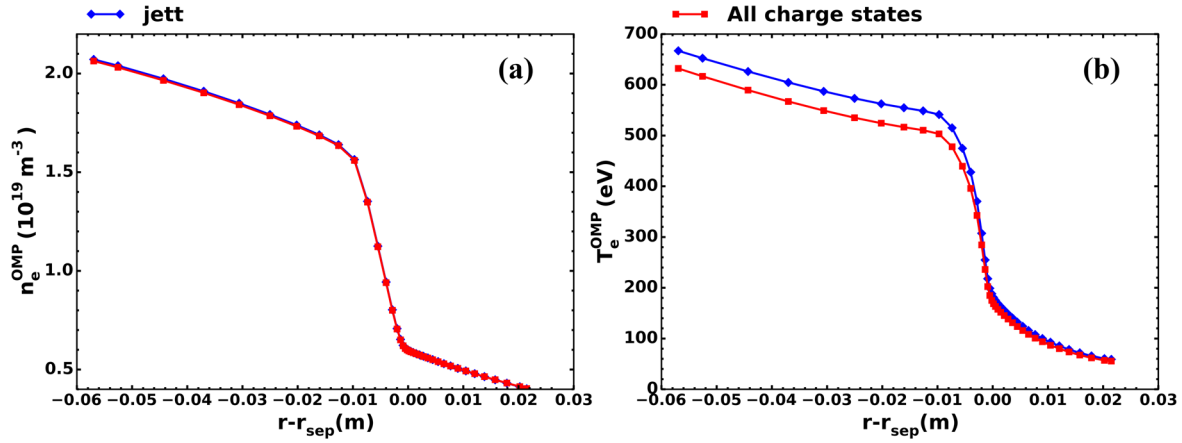

Figure 3. Profiles of n_e^{OMP} (a) and T_e^{OMP} (b) along the OMP in 'jett' and all charge states models, respectively.

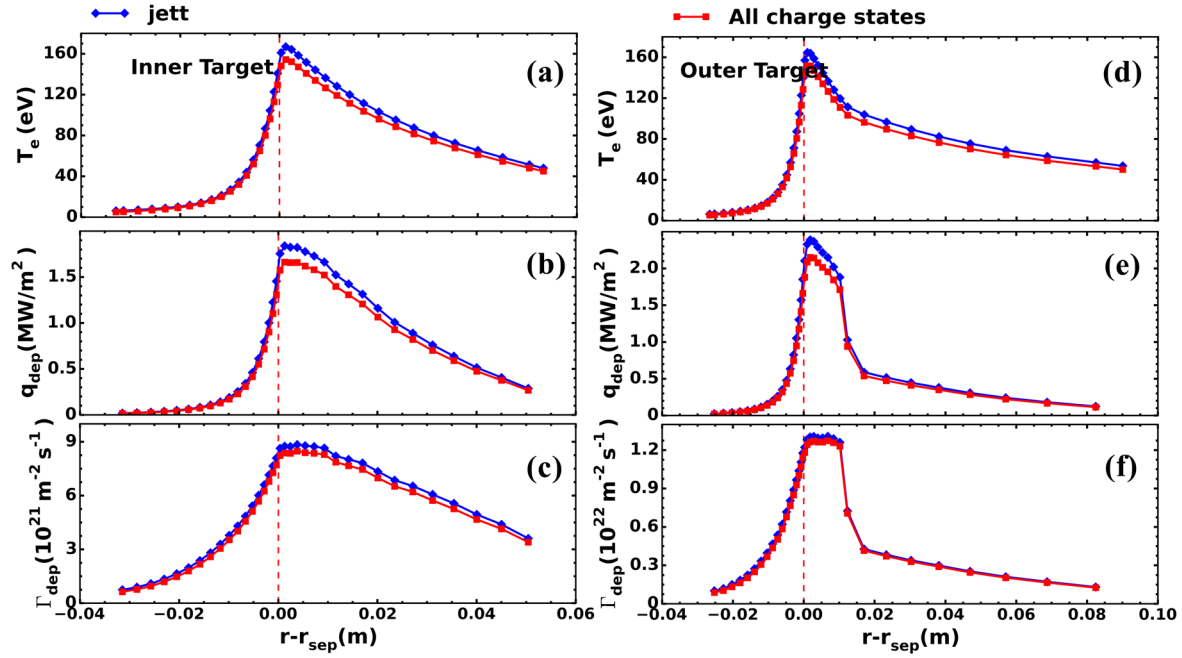

Figure 4. Profiles of T_e ((a) and (d)), q_{dep} ((b) and (e)) and Γ_{dep} ((c) and (f)) along inner target and outer target, respectively.

Table 2. Radiation and W concentration for different models.

		Radiation power loss (kW)					
Model		Core	SOL	Inner divertor	Outer divertor	Total	$C_{sep,w}$ (10^{-3})
All charge states	Ne	20.1	7.0	1.2	4.0	32.3	1.24
	W	177.9	11.1	12.4	13.1	214.5	
jett	Ne	20.0	7.1	1.1	3.9	32.1	1.54
	W	111.7	6.1	7.3	7.8	132.9	

in the divertor and the SOL region. For radiation power loss of W, there is an obvious discrepancy between the radiation of the 'jett' model and that of the all charge states model. It is affected by the bundling scheme especially for the relatively high charge states. The W concentration of the OMP at the separatrix ($C_{sep,W}$) is as high as 10^{-3}. $C_{sep,W}$ of 'jett' is higher than full W treatment, which is no more than 24.5%.

Figure 5 shows W ion density of different charge states for 'jett' and all charge states models at OMP. The density of low charge states W^{1+}–W^{20+} is lower in the 'jett' model than in the all charge states model. The estimation of radiation power loss in the 'jett' model is lower than that in the full W treatment illustrated in table 2. Considering the higher T_e^{OMP} inside the separatrix of 'jett', the density of the high charge

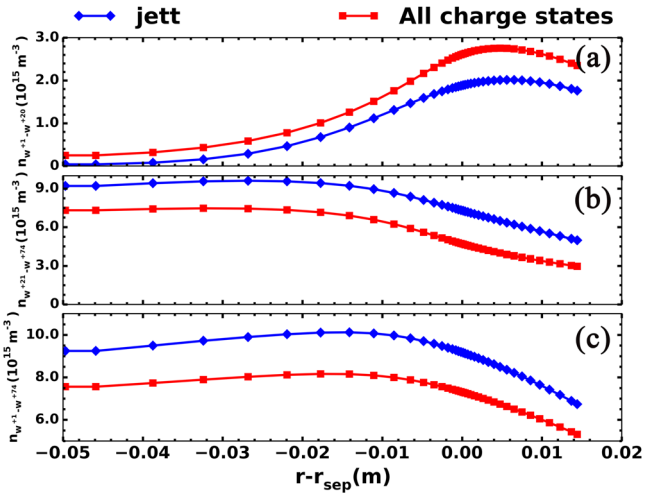

Figure 5. Profiles of W ion density for W^{1+}–W^{20+} (a), W^{21+}–W^{74+} (b) and W^{1+}–W^{74+} (c) along the OMP.

state W^{21+}–W^{74+} is higher than that of the full W treatment, which also results in larger $C_{sep,W}$, as shown in table 2.

The eroded fluxes of W species at the targets are contributed by D, Ne and W species due to their higher incident energy than the sputtering energy threshold of W material. The formula of eroded W flux, Γ_W^{Ero}, is expressed as follows. W physical sputtering yield $Y_{W,phy}$ is calculated by using semi-empirical formula [19–24], which is influenced by incident energy and incident particle species.

$$\Gamma_W^{Ero} = \Gamma_{ion} Y_{W,phy} \tag{1}$$

$$Y_{phy}(E_0) = QS_n(\varepsilon)\left[1 - \left(\frac{E_{th}}{E_0}\right)^{\frac{2}{3}}\right]\left(1 - \frac{E_{th}}{E_0}\right)^2 \times(\cos\partial)^{-f}\exp\{f[1-(\cos\partial)^{-1}]\cos\partial_{opt}\} \tag{2}$$

where E_0 is the incident energy, E_{th} is the energy threshold, Q is the yield factor, S_n represents the nuclear stopping cross section, and ∂ is the incident angle which is assumed to be an average of 45° in the work [25]. Besides, f and ∂_{opt} are fitting parameters. Γ_{ion} is the corresponding particle flux.

To evaluate the level of W sputtering, the eroded W fluxes (Γ_W^{Ero}) by different ions are plotted and compared in figure 6. The total Γ_W^{Ero} of 'jett' is higher than that of the all charge states model due to higher incident energy, which is within 24.5% at the targets. Deuterium ions also make contributions to Γ_W^{Ero} owing to high deuterium particle flux and incident energy. Γ_W^{Ero} from W species is more than one order of magnitude higher than those from D and Ne species. Discrepancies of Γ_W^{Ero} for different models are mainly from D and W species at both targets, which are no more than 24.5% and 22.0%, respectively, at peak values. Γ_W^{Ero} by Ne ions concentrates mainly at the far SOL region due to high Ne particle flux near the puffing location. The bundled model 'jett' shows good consistency with the all charge states model by comparing Γ_W^{Ero} from Ne ions in figures 6(b) and (e). In general, the bundling model 'jett' would not greatly influence the distribution of the Ne impurity.

3.2. W sputtering with varied Ne seeding rate

We also scan the Ne puffing rate by varying the values of $\Gamma_{Ne} = 5.0\times10^{18}$, 1.0×10^{19}, 2.0×10^{19}, 3.0×10^{19} and 4.0×10^{19} atoms/s with deuterium density $n_{D^+,CEI} = 3.0\times10^{19}\,m^{-3}$. As the atom rate of seeding increases from 5.0×10^{18} to 4.0×10^{19} atoms/s, the SP values of T_e, q_{dep} and Γ_{dep} at both targets are shown in figure 7. Γ_{dep} increases, while T_e decreases, as the Ne puffing rate increases. The value of q_{dep} depends not only on Γ_{dep} and T_e, but also on the power entering into the divertor region and divertor radiation [26]. Γ_{dep} and T_e play important roles since the net power in the divertor region is very similar. When the impurity seeding rate is small, T_e is still high, and increased Γ_{dep} plays the main role. q_{dep} at inner SP increases as the seeding rate increases from 5.0×10^{18} to 1.0×10^{19} atoms/s. When the seeding rate increases further, the reduction of T_e becomes the important role, thus, q_{dep} gradually reduces when the seeding rate is higher than 1.0×10^{19} atoms/s, as shown in figure 7(b). But q_{dep} at the outer SP shows a different trend, which declines gradually, as shown in figure 7(e) for the entire range of Ne seeding rates. The divertor operational regime ranges from high recycling regime to detachment as the Ne puffing rate increases. When the plasma temperature is very low ($\leqslant$5 eV) at the divertor targets, the divertor is defined as a detachment. It can be observed that the particle flux rolls over near the SP. When the seeding rate exceeds 3.0×10^{19} atoms/s, the detachment of the outer SP is achieved, firstly with T_e lower than 5 eV, due to more closed geometry for the outer divertor. The peak error of SP values is less than 11.0% at both targets between the two models, which reduces greatly with the increase in Ne seeding rate.

Γ_W^{Ero} for the seeding rates $\Gamma_{Ne} = 5.0\times10^{18}$ and 4.0×10^{19} atoms/s at both targets are presented in figures 8 and 9, respectively. Impurity seeding could affect the sputtering and distribution of W impurity. Total W impurity sputtering around SP reduces gradually due to the lower T_e at the targets as the Ne puffing rate increases. W sputtering from deuterium ions is much less in the high recycling regime, therefore, Γ_W^{Ero} induced by deuterium ions is not shown here. When the Ne seeding rate is not sufficient to suppress W erosion, W self-sputtering plays an important role for total Γ_W^{Ero}, as indicated in figures 6 and 8. W sputtering is gradually dominated by Ne species, with the increase in Ne seeding rate ($\Gamma_{Ne} \geqslant 2.0\times10^{19}$ atoms/s) shown in figure 9. The discrepancy in Γ_W^{Ero} distributions, with different puffing rates shown in figures 8 and 9 between full W charge state mode and 'jett' bundled model, is negligible around SP.

Figure 10 demonstrates the distribution of W density from different divided ranges, and C_W for high seeding rate $\Gamma_{Ne} = 4.0\times10^{19}$ atoms/s. Low-lying states mainly concentrate in the plasma edge. Good consistency is obtained for the distribution of W density between the bundled model 'jett' and full W treatment in the high seeding rate, especially for W ions with low charge states dominantly concentrated in the divertor and the SOL region, as shown in figures 10(a) and (b). The main differences in the ions above W^{20+} are found in the core region due to the low resolution for high charge

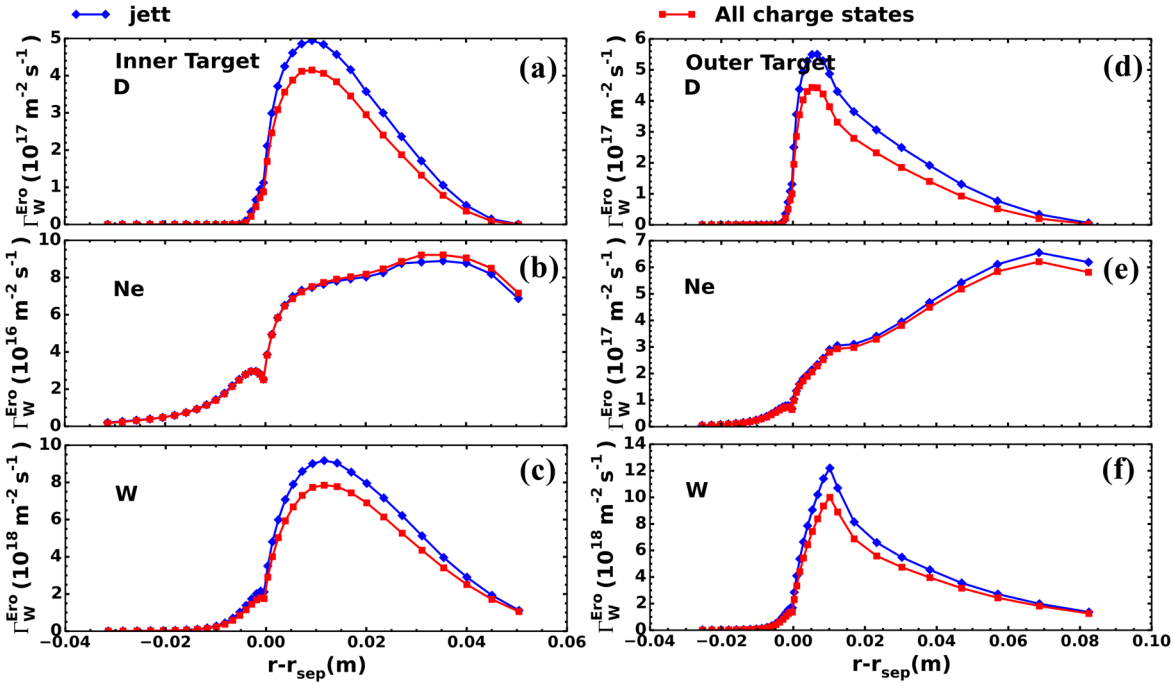

Figure 6. Profiles of Γ_W^{Ero} by D ion ((a) and (d)), Γ_W^{Ero} by Ne ions ((b) and (e)) and Γ_W^{Ero} by W ions ((c) and (f)) along inner target and outer target, respectively.

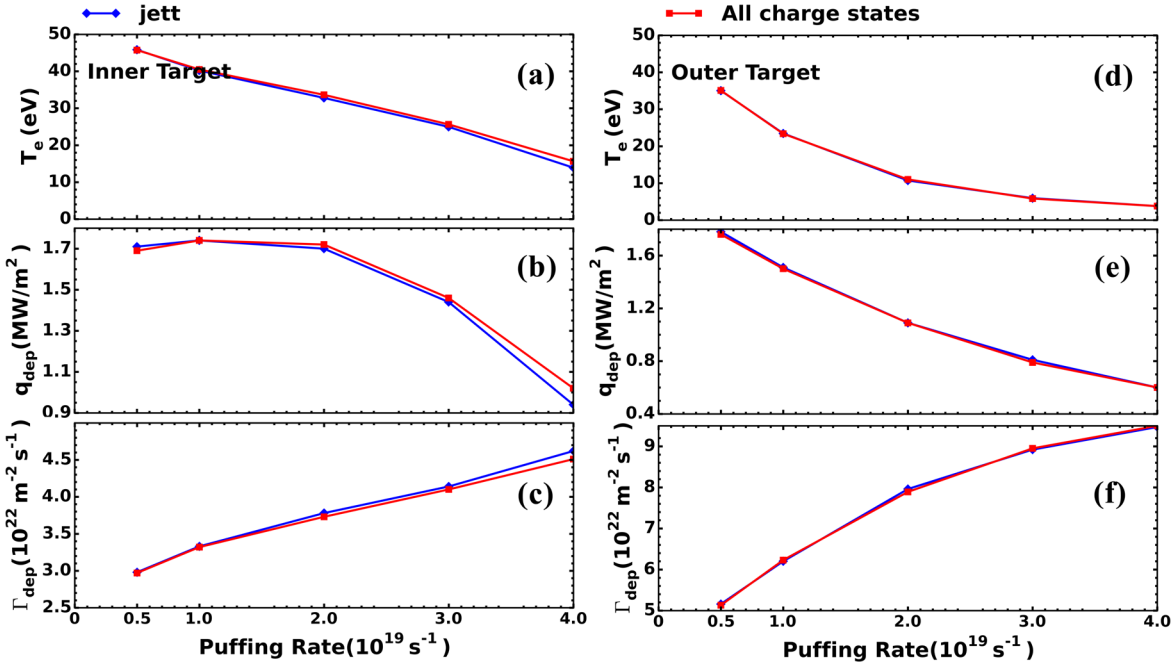

Figure 7. SP values of T_e ((a) and (d)), q_{dep} ((b) and (e)) and Γ_{dep} ((c) and (f)) along inner target and outer target, respectively, as functions of Ne puffing rate.

states of the bundled model, which would not result in a significant influence on the divertor plasma behaviors. Besides, it can be seen that C_W is generally as low as 10^{-5} inside the separatrix shown in figures 10(g) and (h). The sputtered W impurity at the far SOL region of targets is dominant, while it is relatively lower around SP in the high seeding rate due to low T_e.

3.3. Influence of transport diffusivity on W sputtering

Generally, radial particle and thermal transport diffusivities are inverted by the plasma profiles, mostly because it is difficult to measure the transport diffusivities in many present tokamak experiments. BOUT++ transport code is widely used to predict the impact of radial transport diffusivities on

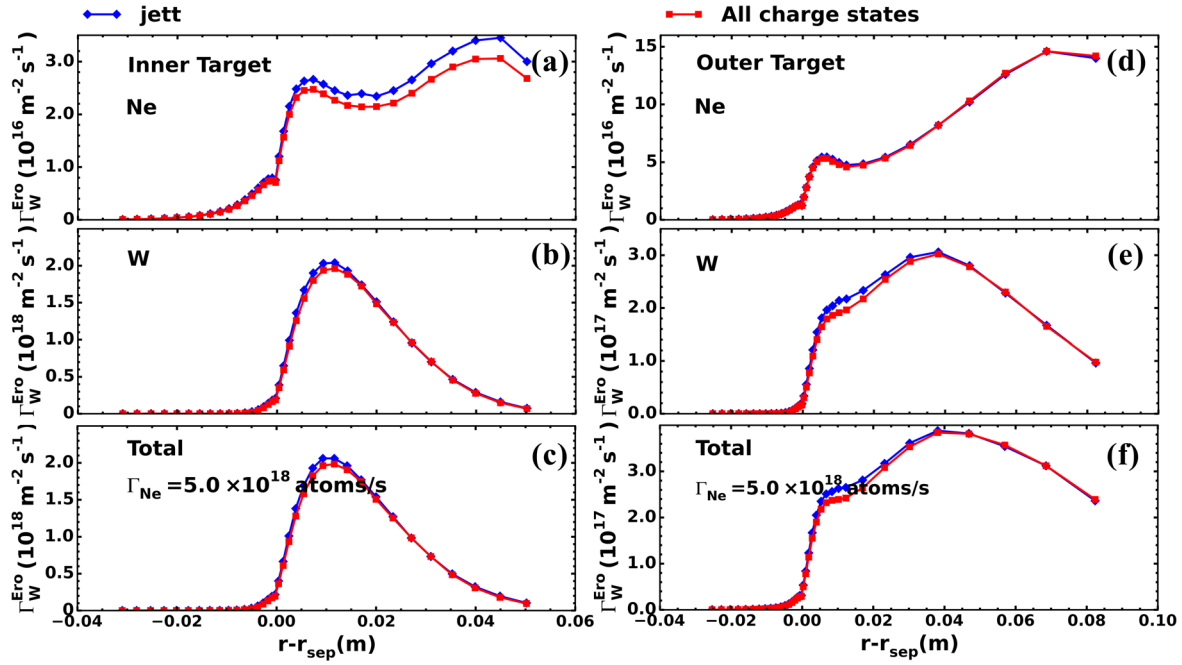

Figure 8. Profiles of Γ_W^{Ero} by Ne ions ((a) and (d)), Γ_W^{Ero} by W ions ((b) and (e)) and total Γ_W^{Ero} ((c) and (f)) along inner target and outer target, respectively, for $\Gamma_{Ne} = 5.0 \times 10^{18}$ atoms/s.

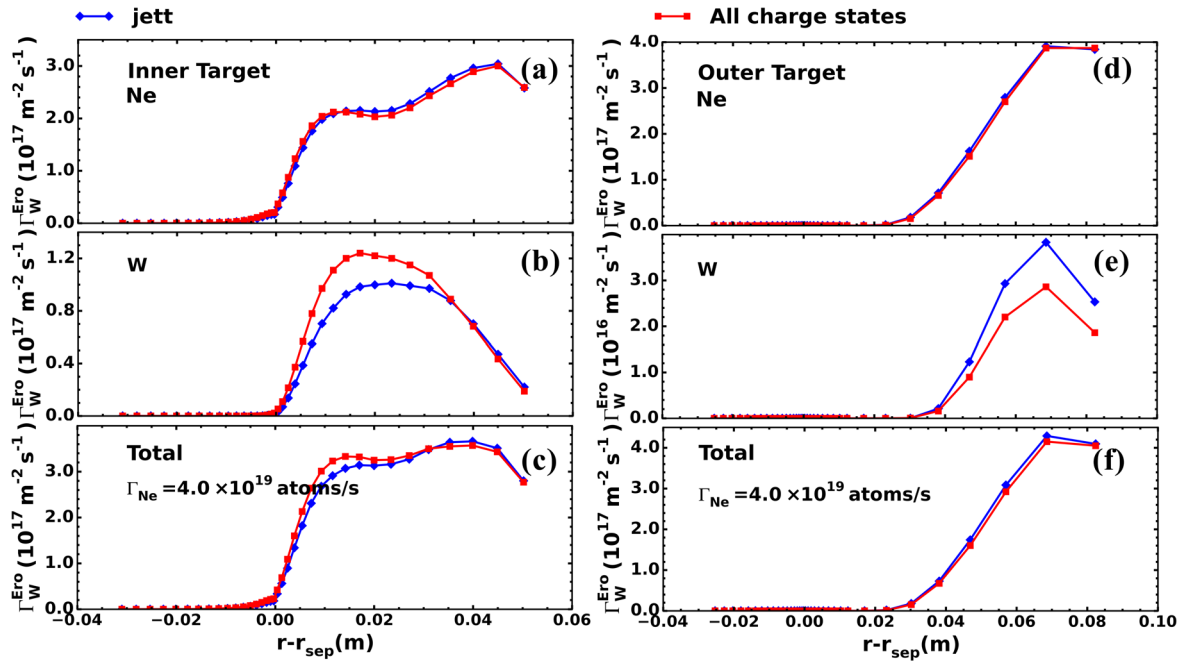

Figure 9. Profiles of Γ_W^{Ero} by Ne ions ((a) and (d)), Γ_W^{Ero} by W ions ((b) and (e)) and total Γ_W^{Ero} ((c) and (f)) along inner target and outer target, respectively, for $\Gamma_{Ne} = 4.0 \times 10^{19}$ atoms/s.

SOL particle and heat flux widths under different mechanisms [27, 28]. The magnitude of decay width of plasma characteristic parameters at targets mainly depends on the radial anomalous transport diffusivities in SOLPS-ITER [29], which could affect the divertor plasma behaviors to a large extent. Therefore, we evaluate the influence of transport diffusivities varied within a certain range on divertor parameters and W impurity sputtering behaviors in this subsection.

We assume diffusivities to be the same inside the separatrix and conduct a scan of diffusivities in the SOL with $n_{D^+,CEI} = 3.0 \times 10^{19}$ m^{-3} and a Ne seeding rate of 1.0×10^{19} atoms/s. Particle and thermal diffusivities in the SOL vary over the range 1.0 to 5.0, which is shown in figure 11. Ion thermal diffusivity χ_i is set to be the same value as electron thermal diffusivity χ_e. When $\chi_{i,e}$ remains fixed at 1.0 in the SOL, $D_\perp$ is scanned from 1.0 to 5.0. Then $\chi_{i,e}$ takes

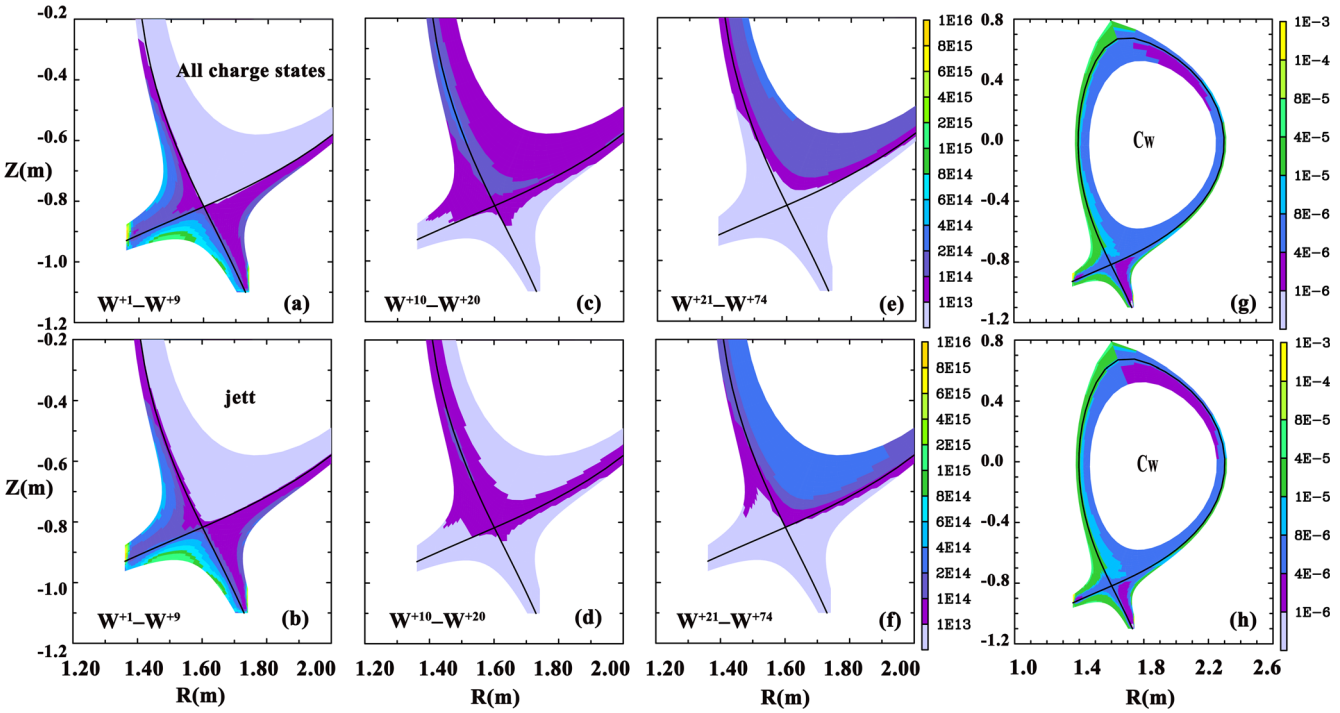

Figure 10. Density of W^{1+}–W^{9+} ((a) and (b)), W^{10+}–W^{20+} ((c) and (d)), W^{21+}–W^{74+} ((e) and (f)) and C_W ((g) and (h)) in all charge states and 'jett' models, respectively, for $\Gamma_{Ne} = 4.0 \times 10^{19}$ atoms/s.

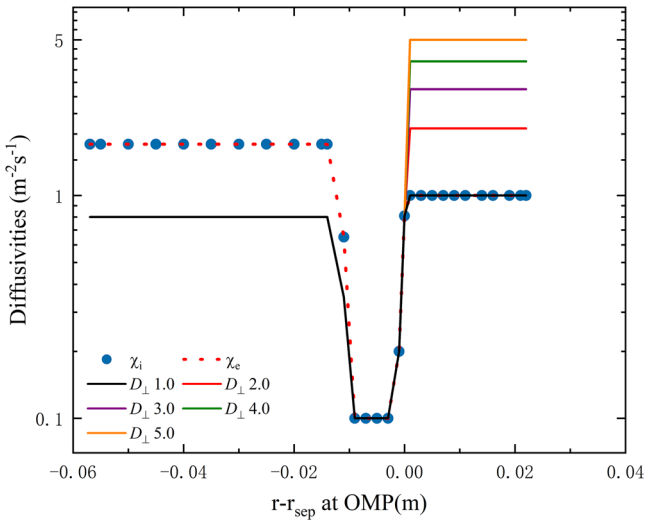

Figure 11. Radial particle and thermal diffusivity setting and scan in SOL.

the same scanning when $D_\perp$ keeps fixed to 1.0 in the SOL. We keep other input parameters the same. The simulations are only conducted by the 'jett' model in this subsection, based on the reasonable agreement results achieved by the model as described above.

Plasma parameters T_e, q_{dep} and Γ_{dep} at divertor targets by scanning $D_\perp$ are shown in figure 12. For simulation with fixed density and particle transport diffusivity at the inner boundary, the number of particles in the simulation domain is fixed at a certain level, and more particles and energy loss at the outer boundary mean less particles and energy to the divertor region. The radial particle transport is enhanced with the increase of $D_\perp$ in the SOL, resulting in an enhanced particle loss at the SOL boundary. One can see that as $D_\perp$ increases in the SOL, Γ_{dep} decreases significantly at the divertor targets, and thus the reduction of q_{dep}. Meanwhile, T_e increases which results in the increase in incident energy.

Figure 13 shows the profiles of total Γ_W^{Ero} at divertor targets. Γ_W^{Ero} is determined by Γ_{ion} and $Y_{W,phy}$, as indicated in equation (1). As $D_\perp$ increases, $Y_{W,phy}$ increases due to the increment in incident energy but Γ_{ion} decreases, as shown in figure 12. Therefore, the competition between Γ_{ion} and $Y_{W,phy}$ determines the final value of total Γ_W^{Ero}. It can be seen that total Γ_W^{Ero} increases with the increase in $D_\perp$. Besides, the erosion of the outer target is more severe than that of the inner target due to the relatively high incident particle flux. The divertor regime for diffusivity $D_\perp = 1$ is in the high recycling regime, which is different from other scans in the low recycling regime. It shows relatively small Γ_W^{Ero} compared with other scans shown in figure 13. The peak erosion rate increases to 0.161 nm s^{-1} with $D_\perp = 5.0$ at the outer target, which means particle diffusivity has a large impact on the W impurity sputtering at the targets.

Figure 14 shows the profiles of T_e, q_{dep} and Γ_{dep} at the divertor targets for which only $\chi_{e,i}$ is varied from 1.0 to 5.0 in the SOL. As $\chi_{e,i}$ increases in the SOL, the thermal transport is increased, resulting in an enhanced energy loss at the SOL boundary. As $\chi_{e,i}$ increases, T_e decreases gradually, resulting in the decrease in incident energy. When $\chi_{e,i}$ exceeds 4.0, the detachment occurs with $T_e \leqslant 5$ eV at the SP of the outer target. The slight influence on Γ_{dep} by varied $\chi_{e,i}$ can be seen in figures 14(c) and (f). Thereby q_{dep} also decreases.

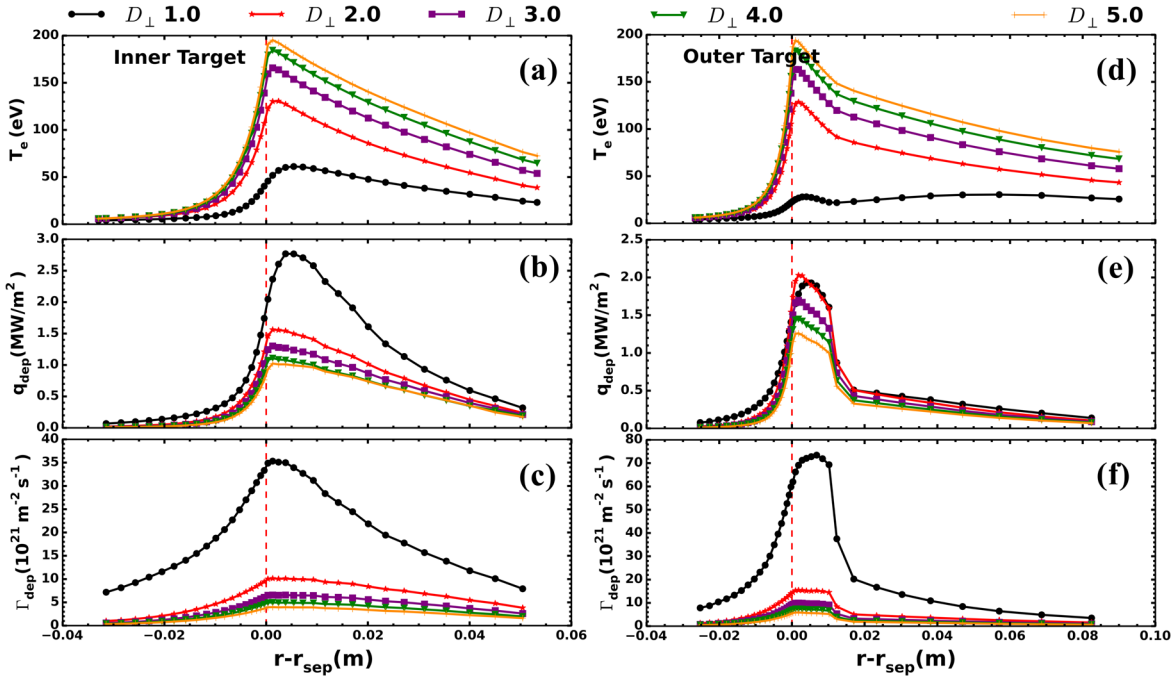

Figure 12. Profiles of T_e ((a) and (d)), q_{dep} ((b) and (e)) and Γ_{dep} ((c) and (f)) along inner target and outer target, respectively.

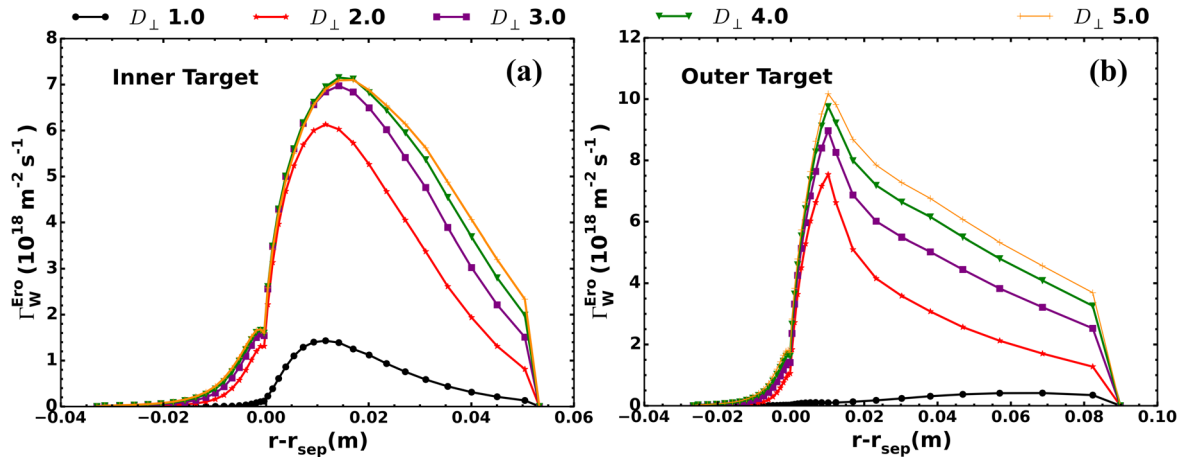

Figure 13. Profiles of Γ_W^{Ero} along (a) inner target and (b) outer target.

The distribution of total Γ_W^{Ero} at the targets is illustrated in figure 15. As $\chi_{e,i}$ increases, Γ_W^{Ero} decreases at the divertor targets, mainly due to the reduction in incident energy. The trend of simulation results by scanning particle and thermal transport diffusivities is consistent with previous works in SOLPS-ITER [30] and BOUT++ code [31], respectively, although the emphasis on detailed comparison is different. The incident energy of deuterium ions is lower than the sputtering energy threshold. Hence, the erosion of atomic W species at targets is mainly contributed by incident Ne and W species. Thermal diffusivity has significant effects on the temperature but a slight influence on particle flux at targets. In general, both radial particle and thermal diffusivities could affect the W impurity sputtering by changing the distributions of temperature and particle flux at the divertor surface.

4. Summary

In this work, the behaviors of W impurity are performed for an H-mode discharge with the EAST updated lower W divertor using SOLPS-ITER code with the bundled charge state model. The highly resolved bundled model 'jett' is selected and evaluated in terms of divertor behaviors and W impurity sputtering with external Ne seeding. The results indicate that the bundled model with high resolution can describe divertor plasma parameters and W impurity behaviors well to a reasonable degree for different divertor operation regimes. It suggests that the W bundling scheme with high resolution in low W charge states ($<W^{20+}$) has little influence on the ionization balance and transport of Ne impurity. There is no significant discrepancy in radiation

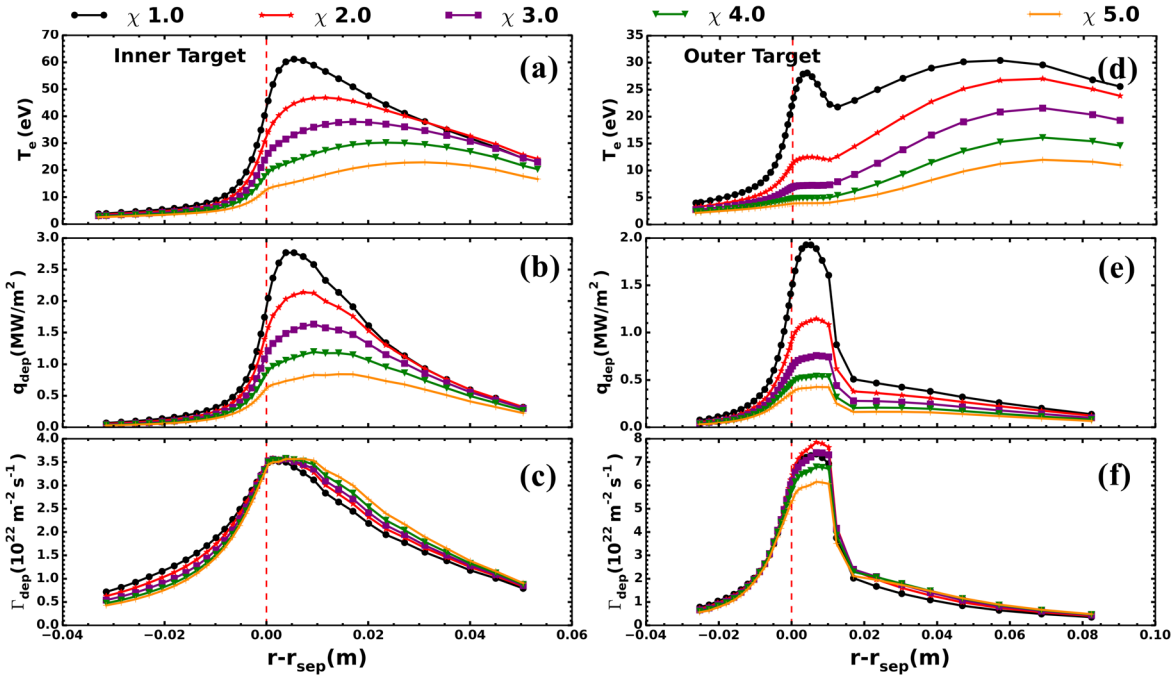

Figure 14. Profiles of T_e ((a) and (d)), q_{dep} ((b) and (e)) and Γ_{dep} ((c) and (f)) along inner target and outer target, respectively.

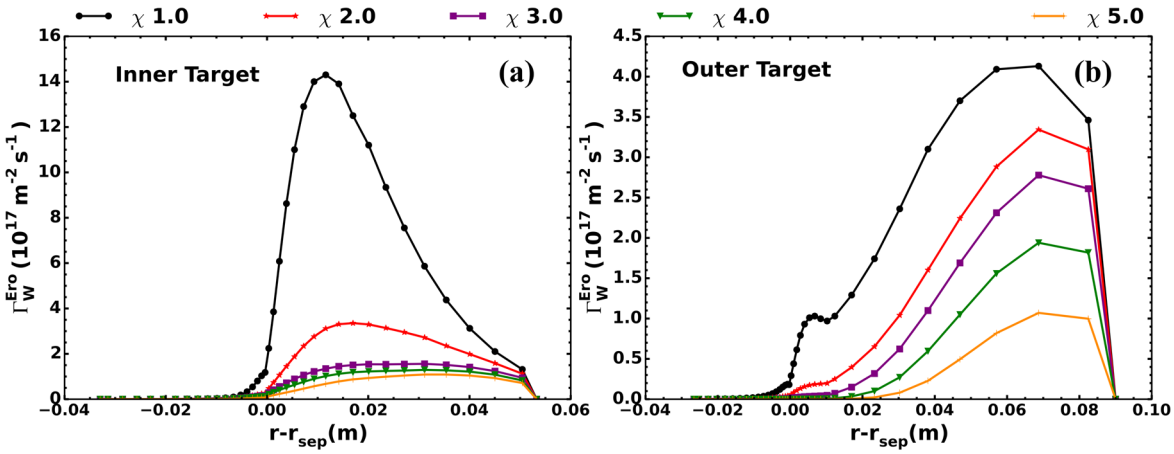

Figure 15. Profiles of Γ_W^{Ero} along (a) inner target and (b) outer target.

power loss and Γ_W^{Ero} produced by Ne species between the bundled model 'jett' and the all charge states model. Compared to the full W treatment, the peak differences in plasma parameters at targets are less than 18.5%, estimated by the 'jett' model at both divertor targets. There is no obvious difference in total Γ_W^{Ero} at either target, between 'jett' and the all charge states model, during Ne impurity seeding.

In addition, simulation of particle and thermal transport diffusivities, $D_\perp$ and $\chi_{e,i}$ scanning from 1.0 to 5.0 only in the SOL, with fixed density at the inner boundary, is conducted by the model 'jett'. As $D_\perp$ increases, Γ_{dep} decreases due to more particle loss from the wall and induces the increase in T_e at the divertor targets, which leads to the increase in Γ_W^{Ero}. However, T_e at the targets decreases gradually with increasing $\chi_{e,i}$ in the SOL due to more heat flowing to wall, which results in the decrease of Γ_W^{Ero}. The change in transport diffusivity has a significant influence on the divertor parameters. Particle diffusivity tends to have a more pronounced effect on the target sputtering than thermal diffusivity.

Drift terms are not taken into consideration because of the numerical difficulty and computational limitation. Attention should be paid to understand the underlying mechanisms of drifts based on the bundled charge state model. The influence of drift terms on the distribution of plasma flow and W impurity transport [32, 33] will be investigated in our future work.

Acknowledgments

The authors would like to thank Yilin Wang for her comments and suggestions. This work is supported by National Natural Science Foundation of China (Nos. 12075283 and 11975271).

References

[1] Philipps V 2011 *J. Nucl. Mater.* **415** S2
[2] ITER Physics Expert Group on Divertor *et al* 1999 *Nucl. Fusion* **39** 2391
[3] Liu X J *et al* 2017 *Phys. Plasmas* **24** 122509
[4] Lore J D *et al* 2019 *Plasma Phys. Control. Fusion* **61** 065001
[5] Xu H C *et al* 2018 *IEEE Trans. Plasma Sci.* **46** 1412
[6] Gao S L *et al* 2021 *AIP Adv.* **11** 025233
[7] Bonnin X and Coster D 2011 *J. Nucl. Mater.* **415** S488
[8] Wiesen S *et al* 2015 *J. Nucl. Mater.* **463** 480
[9] Reiter D, Baelmans M and Börner P 2005 *Fusion Sci. Technol.* **47** 172
[10] Kaveeva E *et al* 2020 *Nucl. Fusion* **60** 046019
[11] Sang C F *et al* 2016 *Nucl. Fusion* **56** 106018
[12] Hechtl E, Bohdansky J and Roth J 1981 *J. Nucl. Mater.* **103** 333
[13] Sytova E *et al* 2020 *Phys. Plasmas* **27** 082507
[14] Huang J *et al* 2014 *Plasma Phys. Control. Fusion* **56** 075023
[15] Chankin A V, Coster D P and Dux R 2014 *Plasma Phys. Control. Fusion* **56** 025003
[16] Brooks J N *et al* 2015 *Fusion Eng. Des.* **94** 67
[17] Ding R *et al* 2016 *Nucl. Fusion* **56** 016021
[18] Xie H *et al* 2017 *Phys. Plasmas* **24** 092512
[19] Yamamura Y, Itikawa Y and Itoh N 1983 *Angular Dependence of Sputtering Yields of Monatomic Solids* Report Number IPPJ-AM-26 (Nagoya: Institute of Plasma Physics Nagoya University)
[20] Eckstein W 1997 *J. Nucl. Mater.* **248** 1
[21] Zhao X L *et al* 2020 *Plasma Phys. Control. Fusion* **62** 055015
[22] Wang Y L *et al* 2021 *Plasma Phys. Control. Fusion* **63** 085002
[23] Warrier M, Schneider R and Bonnin X 2004 *Comput. Phys. Commun.* **160** 46
[24] Eckstein W 2008 *Vacuum* **82** 930
[25] Sang C F *et al* 2018 *Phys. Plasmas* **25** 072511
[26] Sang C F *et al* 2020 *Nucl. Fusion* **60** 056011
[27] Deng G Z *et al* 2020 *Nucl. Fusion* **60** 082007
[28] Deng G Z *et al* 2021 *Nucl. Fusion* **61** 106015
[29] Kukushkin A S *et al* 2013 *J. Nucl. Mater.* **438** S203
[30] Meier E T *et al* 2016 *Plasma Phys. Control. Fusion* **58** 125012
[31] Li Z Y *et al* 2019 *Nucl. Fusion* **59** 046014
[32] Chankin A V *et al* 2015 *Plasma Phys. Control. Fusion* **57** 095002
[33] Aho-Mantila L *et al* 2011 *J. Nucl. Mater.* **415** S231